

# Comparative advantages of mechanical biosensors

J.L. Arlett, E.B. Myers and M.L. Roukes\*

**Mechanical interactions are fundamental to biology. Mechanical forces of chemical origin determine motility and adhesion on the cellular scale, and govern transport and affinity on the molecular scale. Biological sensing in the mechanical domain provides unique opportunities to measure forces, displacements and mass changes from cellular and subcellular processes. Nanomechanical systems are particularly well matched in size with molecular interactions, and provide a basis for biological probes with single-molecule sensitivity. Here we review micro- and nanoscale biosensors, with a particular focus on fast mechanical biosensing in fluid by mass- and force-based methods, and the challenges presented by non-specific interactions. We explain the general issues that will be critical to the success of any type of next-generation mechanical biosensor, such as the need to improve intrinsic device performance, fabrication reproducibility and system integration. We also discuss the need for a greater understanding of analyte-sensor interactions on the nanoscale and of stochastic processes in the sensing environment.**

Advances in micro- and nanofabrication technologies are enabling a wide range of new technologies, including the development of mechanical devices with nanosized moving parts. The ability to fabricate such structures using standard wafer-scale semiconductor processing techniques has allowed attention to move from fundamental problems in biological physics and bioengineering towards the development of practical micro- and nanoelectromechanical biosensors that can be produced *en masse*.

In general, mechanical biosensors capitalize on attributes that scale advantageously as physical size is reduced. First, nanoscale mechanical sensors provide exquisite mass resolution — the minimum detectable added mass is proportional to the total mass of the device. Nanoelectromechanical systems (NEMS) have achieved zeptogram-scale mass resolution while operating in vacuum, and nanogram resolution while operating in a fluid environment<sup>1</sup>.

Second, the mechanical compliance of a device — its ability to be displaced or deformed — greatly increases with uniform reduction of its dimensions. Mechanical compliance converts an applied force into a measurable displacement (and is the mechanical analogue of gain in electronic circuits). This enhanced force responsivity opens new opportunities for measuring the minuscule forces that govern biological interactions. For example, nanomechanical sensors can resolve forces of ~10 pN, which is sensitive enough to detect the rupturing of individual hydrogen bonds.

Third, small fluidic mechanical devices can exhibit fast response times. This allows biological processes in fluids to be observed on the timescales of milliseconds or shorter over which stochastic molecular interactions begin to evolve.

Mechanical biosensors can generally be delineated into four broad categories based on the chemical interactions between the sensor and the analyte: (1) affinity-based assays where highly selective target identification and capture is achieved by the employing high specificity (that is, affinity) between the target and the 'functionalization' at the device surface. Highly specific interactions can exist, for example, between antigens and antibodies; (2) fingerprint assays that rely on a multiplicity of less-selective functionalization layers to identify a target through characteristic binding affinities to an ensemble of sensors; (3) separation-based assays where chemical affinities between immobilized species and flowing analytes permit spatiotemporal separation of analytes; and (4) spectrometric assays where, for example,

the mass or optical properties of the target are deduced to enable its identification.

An outstanding challenge in biosensing is to engineer suites of reliable, high-affinity biochemical agents to capture the target biomarkers we are interested in detecting. High affinity binding<sup>2</sup> is based on biological molecular recognition, which generally occurs only in liquid phase. After capture, target detection is ideally performed *in situ*, within the fluid<sup>1,3,4</sup>. However alternative approaches include removing the detector from the fluid (after the targets are captured), and desiccating it before measurement<sup>5</sup>. Detection *in situ* is obviously simpler and immediate, but mechanical sensing in fluid is strongly affected by viscous damping. As described below, this significantly reduces the mass resolution compared with that obtained in gas or vacuum.

Two widely used (non-mechanical) biodetection technologies are lateral flow assays (LFAs) and enzyme-linked immunosorbent assays (ELISAs). LFAs (which are routinely used for urine analysis) provide quick analysis times (~minutes), ease of use and low cost. However, their concentration sensitivity (that is, the lowest concentration at which target detection is possible) is only ~0.1 µM, which is not good enough to detect many targets of biological importance. By comparison, ELISA requires a much longer analysis time (~1 hr), but it offers much better concentration sensitivity (~1 pM).

Achieving optimal performance for both metrics — an analysis time of less than one minute, and a concentration sensitivity (also known as limit of detection) on the picomolar level or better — is a critical challenge for any new biosensor. Equally important for real applications are practical considerations: can the new technology be mass produced? Can it be integrated with other system components? Can the design of the overall system be kept simple?

In addition to the four chemistry-based categories outlined above, mechanical biosensors can be subgrouped according to the physical processes that underpin their operation. These are described in the next section. Figure 1 and Table 1 summarize the analysis times and sensitivities of the various existing and emerging biosensing technologies discussed in this Review.

## Different types of mechanical biosensor

The central element in many mechanical biosensors is a small cantilever that is sensitive to the biomolecule of interest: such devices can either be surface-stress sensors or dynamic-mode sensors. We will

Kavli Nanoscience Institute and Departments of Physics, Applied Physics, and Bioengineering, California Institute of Technology, MC 149-33 Pasadena, California 91125, USA. \*e-mail: roukes@caltech.edu

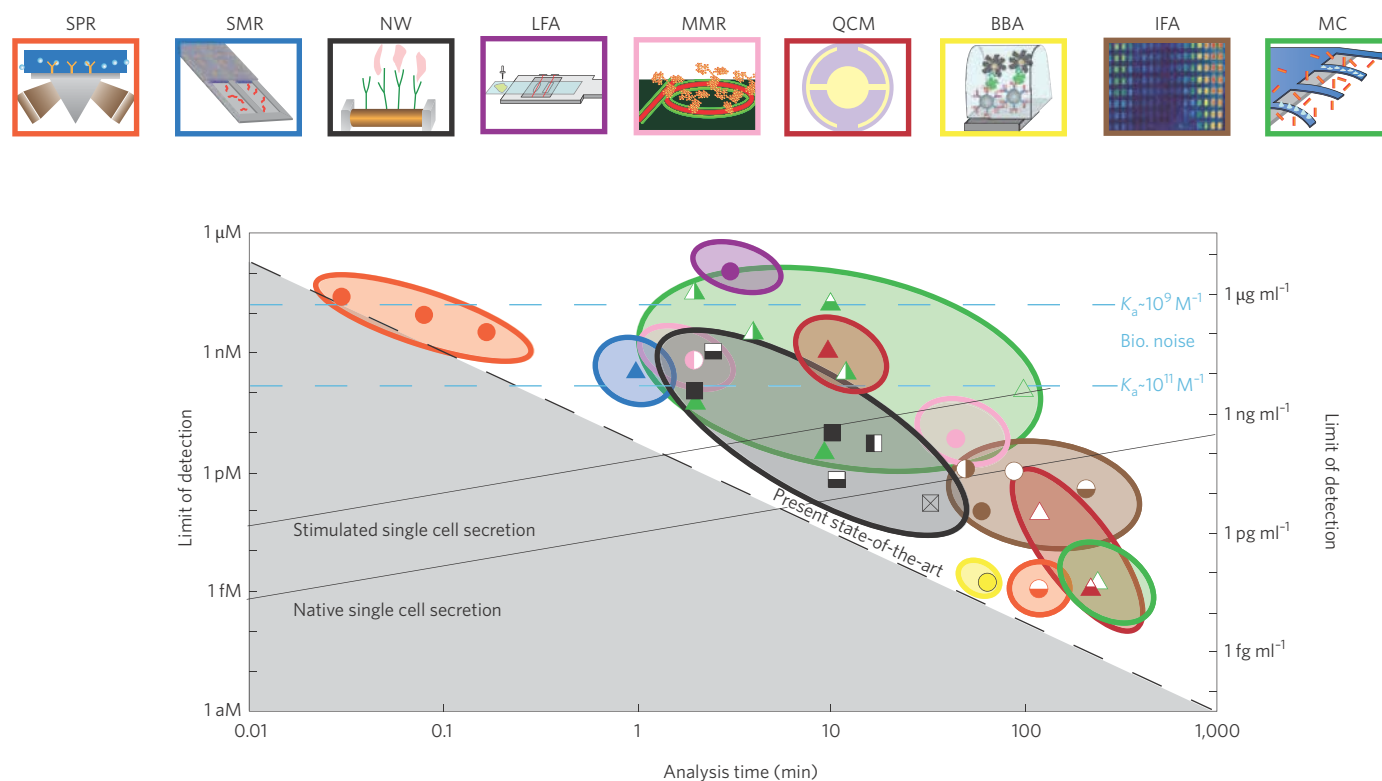


**Figure 1 | Fluidic detection limits for protein sensing.** The limit of detection in moles (left axis) and grams per millilitre (right axis) versus the analysis time for the different types of biosensor (both mechanical and non-mechanical) shown in the panels at the top of the figure and listed in Table 1. Note that both axes are logarithmic. The black dashed line shows the present state-of-the-art (with longer analysis times leading to lower limits of detection); the ideal biosensor would offer low limits of detection and short analysis time (that is, it would be found in the bottom left region of this graph). For many biomarkers the diagnostic level of significance is within the picomolar to nanomolar range, which can be accessed by conventional immunofluorescence assays (IFAs): the challenge for new biosensors is to achieve this sensitivity while also achieving shorter analysis times than the IFA approach. However, detector performance is frequently limited by non-specific binding effects rather than the intrinsic biosensor performance (see text). Non-specific binding effects lead to a 'biological noise floor' below which the analyte of interest cannot be detected. The figure shows the biological noise floors (horizontal blue lines) for target-receptor affinities of  $1 \text{ nM}^{-1}$  and  $100 \text{ nM}^{-1}$  and a non-specific binding association rate of  $10^4 \text{ M}^{-1}$ ; this noise floor is less of a problem when the target-receptor affinity is high. Such limitations do not apply to sandwich-type assays (see text). Many microfluidic sensors are now approaching the level of sensitivity that will permit real-time measurements on proteins secreted from individual cells. The figure shows the biosensor performance (solid black sloping lines) needed to detect the secretion of TNF- $\alpha$  from a single human monomyelocytic cell in a 1-nl volume<sup>121</sup> for both native single cell (SC) secretion and stimulated SC secretion (in which the rate of secretion is increased by a factor of  $\sim 80$ ); a mass of 34 kDa was used to relate concentration to density. SPR: surface-plasmon resonance; SMR: suspended microchannel resonator; NW: nanowire; LFA: lateral flow assay<sup>129</sup>; MRR: microring resonator; QCM: quartz crystal microbalance; BBA: biobarcode amplification assay; IFA: immunofluorescent assay; MC: microcantilever. Panels at top of figure reproduced with permission from: SMR, ref. 37, © 2007 NPG; NW, ref. 128, © 2005 NPG; MRR, ref. 130 © 2009 ACS; IFA, ref. 61, © 2004 RSC.

also discuss quartz crystal microbalances and some non-mechanical biosensors.

**Surface-stress mechanical biosensors.** These devices measure the quasistatic deflection of a miniature mechanical device, usually a cantilever, caused by biomolecules binding to functional groups on the surface of the device (Fig. 2a). As the biomolecules bind, surface stress is developed — owing to electrostatic repulsion or attraction, steric interactions, hydration and entropic effects — and this can induce deflection of the mechanical element. Reference 6 contains a detailed analysis of the relationship of surface stress to surface free energy. Binding of protein<sup>4</sup>, DNA<sup>7–9</sup> and mRNA<sup>10</sup> have been studied, as have drug interactions<sup>11</sup> and conformational changes of proteins<sup>12</sup> and DNA<sup>13</sup>. The amount of deflection is usually measured by reflecting a laser beam off the cantilever, but electrical (piezoresistive) read-out has been employed to measure binding of proteins<sup>14</sup> and DNA<sup>15</sup>. Individual microcantilevers are susceptible to parasitic factors that accompany their exposure to a sample aliquot; spurious deflections from proximal changes to index of refraction, temperature and fluidic

disturbances can result. These can be partially circumvented by differential measurements<sup>4</sup> that enable *in situ* comparison between the induced strain on cantilevers that have been functionalized and those that have been passivated. Reported sensitivities range from  $\sim 100 \text{ pM}$  (ref. 7) to the few nanomolar range<sup>4</sup> (Fig. 1, Table 1).

Stress within self-assembled monolayers can be deduced from surface-stress sensor measurements through Stoney's formula<sup>16</sup> for devices with large aspect ratio (that is, length:thickness  $> 10$ ). For devices with smaller aspect ratio, the more detailed analysis of Sader<sup>17</sup> must be used.

**Dynamic-mode mechanical biosensors.** These devices are not quasistatic: rather, they oscillate with a resonance frequency, and this frequency changes when molecules land on the cantilever (Fig. 2b). Below we describe different operating environments and different modes of operation for such sensors

**Humid environments.** Real-time monitoring of very small-scale bacterial colonies has been achieved by growing them directly on

**Table 1 | Comparison of the analysis time and limit of detection for different types of biosensors.**

Category	Symbol in Fig. 1	Description	Detection conditions	Reference	Analysis time	Limit of detection
<b>Optical detection</b>						
<b>Label-free real-time detection</b>						
MRR: microring resonator		Label-free detection with a microring resonator	5 protein mixture in BSA-PBS (0.1 mg ml <sup>-1</sup> BSA)	51	2 min	0.6 nM
SPR: surface-plasmon resonance		Label-free SPR detection	0.1 mg ml <sup>-1</sup> BSA	58	10 s	3 nM
<b>End point and/or labelled detection</b>						
LFA: lateral flow assay		Pregnancy test	Urine	129	3 min	10 µM
IFA: immunofluorescent assay		ELISA	Serum		60 min	0.1 pM
		Integrated blood barcode chip (IBBC) with DEAL	Whole blood	62	90 min	1 pM
		Microfluidic fluorescent immunoassay	Cell-culture supernatant	61	45 min	1 pM
		Bead-based microfluidic immunoassay with zM sensitivity	4 protein mixture in PBS with 1% BSA	63	210 min	0.4 pM
MRR: microring resonator		Labelled detection with a microring resonator	IL-2 in BSA-PBS	52	45 min	6.5 pM
BBA: biobarcode amplification assay		Protein amplification via functionalized nanoparticles	Serum	72	45 min	0.5 fM
SPR: surface plasmon resonance		Labelled detection with SPR (DNA detection)	TNE	60	2 h	1.4 fM
<b>Mechanical detection</b>						
<b>Label-free real-time detection</b>						
MC: microcantilevers		Static mode (surface-stress sensors, SSS), functionalized reference	HBST buffer	4	10 min	15 nM
		SSS, unfunctionalized reference, piezoresistive detection	0.1 mg ml <sup>-1</sup> BSA	14	12 min	300 pM
		SSS, no reference cantilever	1 mg ml <sup>-1</sup> HSA	7	100 min	100 pM
		Dynamic mode detection (mass sensing)	PBS	30	12 min	0.3 pM
SMR: suspended microchannel resonator		Protein detection in serum	Serum	3	1 min	300 pM
QCM: quartz crystal monitor		Detection of C-reactive protein	0.1 M sodium phosphate buffer	46	10 min	1 nM
<b>End point and/or labelled detection</b>						
MC: microcantilevers		Mass sensing with liquid phase capture and vapour phase detection	Serum	5	4 h	1.5 fM
QCM: quartz crystal monitor		Mass sensing with liquid phase capture and vapour phase detection	Serum	47	180 min	85 fM
		DNA detection using a sandwich assay with mass amplification	0.4 M phosphate buffer	48	220 min	1 fM
<b>Electrical detection</b>						
<b>Label-free real-time detection</b>						
NW: nanowire		Nanowire FET for DNA detection	Buffer	55	10 min	10 pM
		Nanowire FET for detection of PSA, time domain	Buffer	54	17 min	5 pM
		Nanowire FET for detection of PSA, frequency domain	Buffer	54	33 min	0.15 pM
<b>End point and/or labelled detection</b>						
NW: nanowire		Nanoribbon FET	Whole blood	70	11 min	0.6 pM

The symbols in the second column correspond to the data points shown in Fig. 1. The analysis time (column six) is the total analysis time including incubation steps.

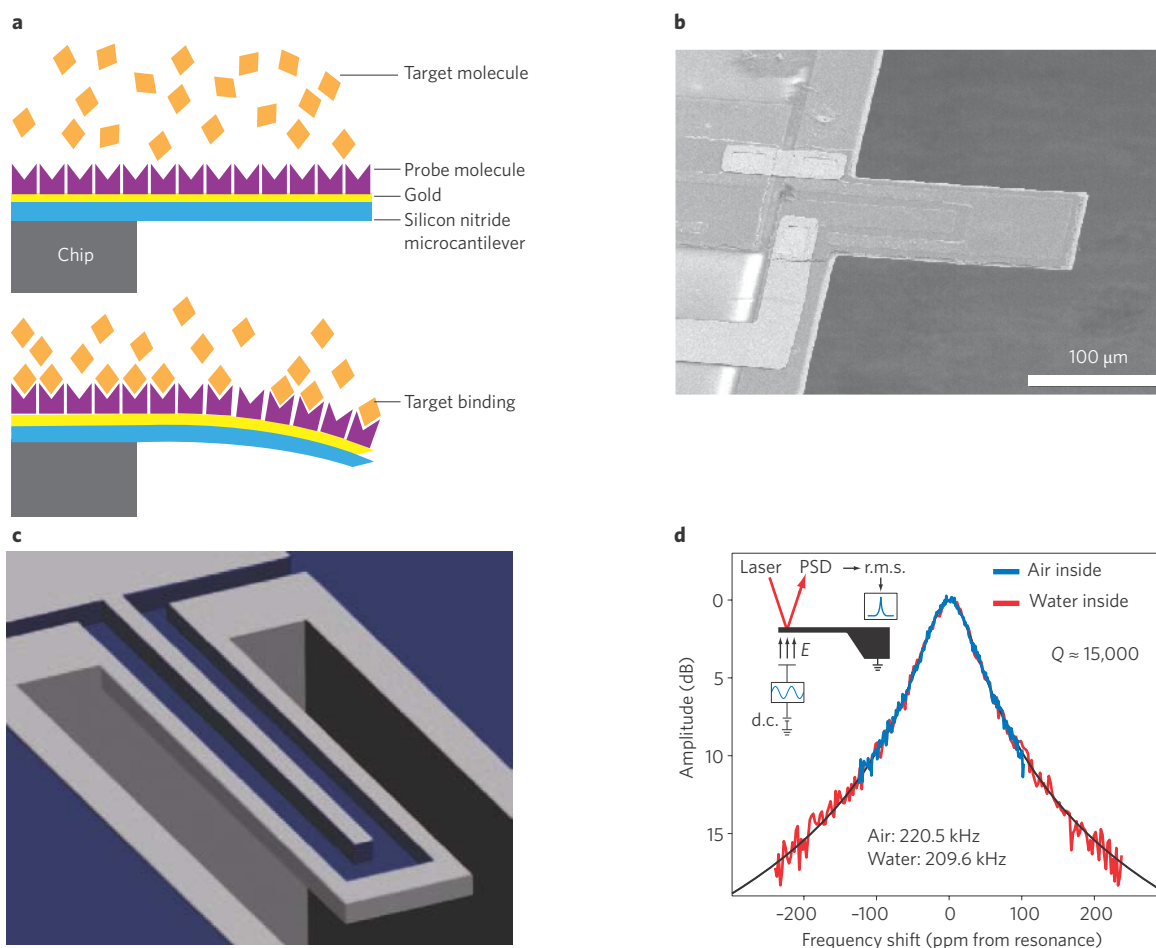


**Figure 2 | Fluidic micromechanical biosensors.** **a**, Schematic of static-mode surface-stress sensing MEMS device. Binding of target molecules generates a surface stress, which leads to a quasistatic deflection of the cantilever (bottom)<sup>7</sup>. **b**, Scanning electron micrograph (SEM) of a dynamic mode MEMS device. Target molecules are detected through their influence on the resonance frequency of the cantilever: when the molecules land on the cantilever, they increase its mass and therefore reduce its resonance frequency<sup>25</sup>. **c**, Suspended microchannel resonator (SMR). The fluid containing the target molecules flows through a channel inside the device (the top of the device is not shown in this cutaway schematic) and bind to the inner flow-channel walls, while the resonator oscillates in air or vacuum<sup>3</sup>. **d**, Resonance spectrum (oscillation amplitude versus frequency) of a SMR. The quality factor of the device is normally unaffected when the channel is filled with water (red line)<sup>37</sup>. Figure reproduced with permission from: **a**, ref. 7, © 2001 NPG; **b**, ref. 30, © 2004 RSC; **c**, ref. 3, © 2010 ACS; **d**, ref. 37, © 2007 NPG.

micromechanical mass sensors. This involves maintaining the devices in a humid, gas-phase environment, but obviates the need for their direct immersion in fluid. Monitoring growth of *E. coli* microcultures in less than one hour<sup>18,19</sup> has been demonstrated, which compares favourably with ~ one day times for conventional methods. Moreover, the detection of antibiotic selective growth has been made in less than two hours<sup>19</sup>. This approach offers potential for simultaneous multiplexed detection of various bacterial species through device arrays.

**Fluid-phase capture and detection in vacuo.** Mechanical biosensors can provide exquisite mass resolution in vacuum and in air<sup>20,21</sup>. An approach that harnesses this level of performance for fluidic biosensing involves operating the device in solution, removing it from solution once the analytes have bound, then desiccating them before mass detection. However, spurious molecules can bind to the device during desiccation, which leads to errors (and continuous monitoring is not possible — see below). Early efforts in this area focused on the detection of relatively massive virus particles<sup>22,23</sup>, and single-virion resolution was achieved<sup>22</sup>. More recently, a ‘sandwich assay’ was used to detect prostate-specific antigen (PSA) in serum at femtomolar concentrations<sup>5</sup>. Sandwich assays employ two affinity-based probes (often two different antibodies) to achieve an effective affinity that is the product of the affinities of the individual

agents. A label is often attached to the second probe to enable the readout (for example, fluorescent assays) or to enhance the signal (for example, labelling with relatively massive nanoparticles for mass-based detection<sup>5</sup>).

**Continuous operation.** The method described in the previous section is not capable of continuous monitoring and fast detection. However, if a dynamic-mode mechanical biosensor is immersed in the fluid, continuous monitoring with picomolar sensitivity and response times of a few minutes becomes possible. However the concentration sensitivity attained depends on the target mass; subpicomolar detection of T5 virions (molecular weight =  $7 \times 10^7$  Da) is possible<sup>1</sup>, whereas micromolar sensitivity is typical for smaller peptides such as ferri-chrome (molecular weight = 687.7 Da). Dynamic-mode mass sensing has also been used for mass measurements of individual live cells<sup>24,25</sup>.

Sensitive frequency-shift-based mass detection requires resonators with high vibrational quality factors, but the quality factor,  $Q$ , is compromised in fluid by viscous damping<sup>26</sup>. However, high-frequency operation increases the effective Reynolds number and can enable operation with higher values of  $Q$ <sup>27</sup>. These higher frequencies can be achieved by reducing the device dimensions, or by operating with high-order vibrational modes<sup>28,29</sup>. Figure 1 shows the present state-of-the-art performance.



Several groups report discrepancies between adsorbed mass and induced frequency shift, both for liquid-phase<sup>30,31</sup> and gas-phase measurements<sup>32</sup>. This has commonly been attributed to surface stress induced by the adsorbates, yet theoretical estimates of expected magnitudes are far smaller than what is observed. This is especially true for the case of microcantilever sensors, where simple extension or contraction can relieve surface stress<sup>33</sup>. 'Strain-dependent' surface-stress models have been proposed<sup>33</sup> but their validity is questioned<sup>34</sup>. It has been shown<sup>34</sup> that clamping effects can significantly affect surface stresses developed in short cantilevers but, again, the expected stress-induced frequency shifts are smaller than experimental observations.

Adsorbed analytes can also potentially induce a frequency shift by changing the composite elasticity of the sensor. It has been proposed that such changes might dominate the frequency shift induced by mass loading, even when the layer of adsorbed species is much thinner than the device<sup>35</sup>, and both experimental and theoretical evidence have been reported for such a stiffening effect from thin antibody layers on 30-nm-thick microcantilevers<sup>36</sup>.

**Suspended microchannel resonators.** An ingenious alternative to immersing dynamic mass sensors in fluid is to constrain the fluid to channels embedded in the mechanical resonator itself<sup>37</sup>. Such suspended microchannel resonators (SMRs) can be measured *in vacuo* where values of *Q* of up to ~15,000 can be obtained (Fig. 2c,d). Measurements of fluidic dissipation in SMR devices suggest that some *Q* degradation may occur for fluid-filled nanochannels<sup>38,39</sup>, but these results are not fully understood theoretically<sup>40,41</sup>. So far, despite the high values of *Q* attained, the performance of SMR biosensors is modest. The glycoprotein ALCAM has been detected in undiluted serum at 300 pM concentrations in several minutes<sup>3</sup>. In this case the detection limit was set by non-specific binding. (The intrinsic performance should be about two orders of magnitude better than this.) SMRs have been applied to measurements of cell mass and density during the cell cycle of yeast<sup>42,43</sup> and have been used to measure growth rates from single cells both for bacterial and mammalian cells<sup>43</sup>. They have also been used for detection of antibiotic resistance<sup>44</sup>. Elsewhere we have carefully analysed the ultimate practical limits to SMR biosensing<sup>45</sup>.

**Other mechanical biosensors.** There is one other widely used mechanical biosensor — the quartz crystal microbalance — and also a variety of non-mechanical biosensors, including whispering-gallery microcavity resonators, optical microring resonators and nanowire biosensors.

**Quartz crystal microbalances (QCM).** These are centimetre-scale mechanical resonators that can measure the inertial mass of analytes accreting on their surfaces in vacuum, gas or fluid. A downshift in the resonant frequency occurs with target accretion, which is most reliably tracked electronically, in real time. Fluid-based QCM bio-detection spans the nano- to femtomolar range: nanomolar sensitivity is reported for continuous analyte monitoring using an indirect-competitive assay<sup>46</sup>, whereas ~100 fM sensitivity has been reported for end-point detection assays involving device removal from fluid, post-capture drying, and subsequent measurement *in vacuo*. Femtomolar sensitivity is reported by a technique combining this end-point vacuum detection approach with a sandwich assay providing immunospecific target-mass enhancement<sup>47,48</sup>. However, as mentioned, the need to remove samples from fluid and desiccate them before measurements *in vacuo* makes these assays cumbersome and susceptible to measurement artifacts.

**Whispering-gallery microcavity (WGM).** Consists of a high-finesse toroidal optical resonator coupled evanescently to an optical fibre. Adsorption of analytes to the surface of the resonator measurably alters its properties. First efforts reported unprecedented ~100 aM

sensitivity with response times ~1 s (ref. 49), but these results caused significant controversy. The data have not been reproduced, and subsequent analyses suggest they are incommensurate with expected resonance shifts<sup>50</sup> and binding kinetics. Recently, some of the authors of ref. 49 have reported follow-up studies showing reproducible, albeit more conservative, results: detection of the relatively large influenza-A virion at picomolar concentrations within ~10 s (T. Lu *et al.*, manuscript in preparation).

**Optical microring resonators (MRRs).** These devices are similar to WGM devices, but offer the advantage that they can be fabricated by standard methods and, thus, are more readily integrated into multiplexed detection systems. However, this advantage comes at the price of lower optical quality factors and, hence, reduced sensitivity; label-free MRR-based detection is reported in the nanomolar range with response times ~1 min. MRR biosensors have enabled quantification of unknowns from a mixture of five proteins<sup>51</sup>, and sandwich-assay detection yielding ~6.5 pM sensitivity.<sup>52</sup>

**Nanowire biosensors.** The conductance of these devices — which are made from semiconductor nanowires and carbon nanotubes — changes when a target molecule binds to the surface of the device. This 'electrochemical gating' arises from a change in local surface potential induced by target binding or changes in solution pH. Even for nominally similar systems, the concentration sensitivities reported for nanowire biosensors span a large range of values, from the femtomolar<sup>53</sup> to the few-picomolar scale<sup>54,55</sup>. An initial sensitivity of 5 pM can be improved to 0.15 pM through the use of frequency-domain detection<sup>54</sup>, and optimization by subthreshold biasing can improve this further, to 1.5 fM (ref. 56). Some reported results are not consistent with recent estimates of binding kinetics<sup>57</sup> — given the minuscule surface areas available on the surface of a nanowire for binding, estimates suggest that at fM concentrations there should be only one capture event every few days!

Nanomolar sensitivity has also been reported for label-free protein biosensing with surface-plasmon resonance (SPR) biosensors<sup>58</sup> and photonic-bandgap (PBG) biosensors<sup>59</sup>. This level of performance can be improved to the femtomolar range by using sandwich-assay end-point detection (in which label probes incorporating gold nanoparticles that enhance SPR are employed<sup>60</sup>). Optical fluorescence detection methods are routinely used to achieve picomolar sensitivity, but they typically require incubation times on the order of hours<sup>61–63</sup>.

### Sensitivity versus other performance metrics

The detection of rare biomarkers in blood plasma is an archetypal goal for advanced biosensors. For many biomedical targets of interest, existing sensors are capable of reaching the diagnostic level of significance: this is ~4 ng ml<sup>-1</sup> (120 pM) for PSA. A number of other cancer biomarkers have similar thresholds, that is, they are within the sensitivity range of other technologies (Fig. 1). However, there is a clear need for biosensors that can simultaneously detect a number of different biomarkers (that is, fingerprint assays). The case of prostate cancer illustrates some of these challenges: recent studies have shown that 70% of males with PSA levels at or below the current diagnostic level of significance do not develop this form of cancer<sup>64</sup>, so there is a need for better diagnostics.

For biosensor applications, it is necessary to focus on both the intrinsic device performance and on the performance of the overall sensor system. Important considerations include: ease of biofunctionalization and potential for multiplexing; complexity of fabrication and integration; device robustness and shelf life; the trade-off between sensitivity and frequency of false positives<sup>65</sup>; and the readiness and adaptability for production *en masse*.

**Non-specific binding and the biological noise floor.** It is not often appreciated that biosensing is more complex than simply finding 'a

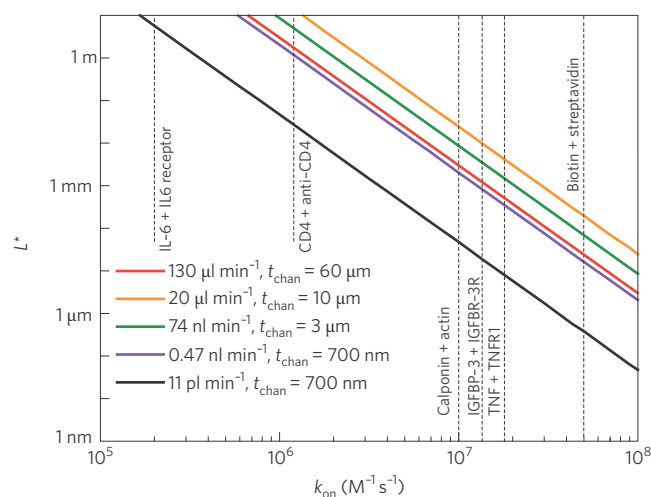


**Figure 3 | Depletion in microfluidic structures.** The length needed for 50% depletion  $L^*$  versus the rate of association  $k_{on}$  in an open-loop fluidic configuration for five different combinations of flow rate and microchannel geometry: details of four of these combinations are shown in Table 2; for the fifth combination (black line)  $t = 700$  nm,  $w = 4$   $\mu$ m and  $l = 2.05$  cm. The dotted vertical lines show the values of  $k_{on}$  for the six target-receptor pairs listed in Table 2. Significant depletion can be achieved for lengths of hundreds of nanometres for very small channels (in which the flow rate is reduced) for the highest values of  $k_{on}$  (such as for biotin-streptavidin binding), but tens of micrometres or more are needed to achieve significant depletion for larger channels (with much greater flow rates), even for the highest values of  $k_{on}$ . For much lower values of  $k_{on}$  (such as IL-6 binding to its receptor) it is not possible to achieve significant depletion within practical length scales for microfluidic sensors, implying that the kinetics are always reaction limited. Depletion length scales shown here are for short timescales, that is, far from equilibrium. Near equilibrium the kinetics are always dominated by reaction kinetics (see Table 2). Depletion is strongly dependent on the flux of molecules to the surface, which depends on both the flow rate and the channel geometry; here depletion has the greatest role for the combination shown by the black line.

needle in a haystack' because of the problem of non-specific binding. Other species are present at much higher concentrations than the target biomolecule (perhaps at concentrations a billion times greater than the target), and these species can also bind to the sensor, which results in most of the sensor interactions being non-specific. Even if the residence times associated with these non-specific binding events are much shorter than those for specific binding events, non-specific interactions impose a fundamental biological noise 'floor' to achievable limits of detection.

We illustrate this problem with a simple hypothetical example. Non-specific interactions can take place at functionalized, passivated and untreated regions of a device; and all can have a role in limiting detection sensitivity. Representative rates of protein association for non-specific binding<sup>66,67</sup>,  $K_a^{NS}$ , typically fall within the range of  $10^4 - 10^5$   $M^{-1}$ , whereas generic target/receptor interactions, such as TNF and TNFR1, have binding affinities  $K_a^S$  of  $\sim 10^{11}$   $M^{-1}$ . Albumin, the most prevalent protein in blood plasma, is present at concentration  $c_{prev} \sim 600$   $\mu$ M. We assume the number of specific and non-specific binding sites of the sensor — represented as  $b_s$  and  $b_{NS}$ , respectively — are comparable, and define the limit of detection as yielding a 3:1 signal-to-background ratio. For the example of TNF in plasma, these considerations result in a background biological noise floor,  $c_{noise} = (3c_{prev}b_{NS}K_a^{NS})/(b_sK_a^S)$ , that is equivalent to  $\sim 1.8$  nM target concentration. Many other targets of interest have much weaker binding affinities and will correspond to higher biological noise levels.

Measurements of ALCAM in serum with suspended microchannel resonators demonstrate that non-specific binding can be central

in determining ultimate detection limits<sup>3</sup>. In these measurements, the practical detection limit (defined as the standard deviation of the response to negative controls) was roughly 200 times worse than expected from the mass resolution of the device. Although non-specific binding is not the only factor that determines this detection limit (the measurements are performed over a period of approximately 20 min, so sensor drift might also have a role), these measurements demonstrate that state-of-the-art technologies have already reached a level where the detection limit is determined not by the intrinsic device sensitivity but by other factors. Understanding and controlling non-specific binding is likely to be key to further gains in sensitivity.

Despite the importance of these considerations, little systematic experimental investigation has been undertaken to quantify biological noise arising from non-specific interactions in practical situations. Nair and Alam have modelled physisorption onto unpassivated regions of devices, assuming the rate constants between non-specific and specific binding differ by a factor of  $10^9$ . Even though this ratio is somewhat arbitrary, their conclusions underscore the importance of dense biofunctionalization surface coverage to achieving high selectivity<sup>68</sup>. Their model indicates that target discrimination remains possible with high coverage of specific receptors ( $\sim 2 \times 10^{12}$   $cm^{-2}$ ), even when other species that we are not interested in are  $10^9$  times more abundant in solution. They suggest discrimination can be enhanced further by back-filling 'voids' in functionalization with, for example, PEG or other biopassivation species. Finally, it has also been shown that differential measurements can be employed to circumvent false positives arising from biological noise<sup>10</sup>.

**Practical signal enhancement.** The limitations imposed by non-specific binding can be overcome, at least in part, at the cost of more complex procedures such as the use of sandwich assays<sup>52,69</sup> to increase target capture specificity. Variations on the traditional sandwich assays can also be used, such as the two-step process used to detect PSA at  $\sim 60$  pM (2ng  $ml^{-1}$ ) in whole blood within  $\sim 20$  min using a nanoribbon sensor<sup>70</sup>.

Another approach is to amplify the target analyte so that its concentration rises above the biological noise floor. The widely used polymerase chain reaction (PCR) exponentially amplifies initial target species and has enabled measurements of DNA from individual cells in volumes  $> 100$   $\mu$ l (ref. 71). At present, protein assays do not achieve such profound species amplification, but enhancement methods have been developed that provide some level of signal amplification. The ELISA assay, perhaps the archetypal example, employs an enzyme bound to a detection antibody. Each enzyme molecule acts as a signal amplifier, typically producing thousands of signal molecules per second. Although the ELISA process provides only a linear (rather than exponential) increase in the signal with time, it can still achieve subpicomolar detection sensitivities (Fig. 1).

Labelling provides another form of signal amplification. A label can serve two purposes: to enhance detection specificity through sandwich-assay mechanisms, and to directly amplify the detected signal. For example, SPR sensors achieve nanomolar-concentration sensitivity in their basic, label-free form (Fig. 1, Table 1). However, substantial enhancement of the induced plasmonic signal, reportedly to enable femtomolar sensitivity, is possible through immunospecific attachment of gold nanoparticles to the target in a final labelling step (although this approach also involved a two-hour incubation period)<sup>60</sup>. Labelling enhancement is possible with optical (MRR) biosensors; 0.6-nM label-free detection within several minutes is typical<sup>51</sup>, and labelled detection with 6.5-pM sensitivity, which enables detection of smaller proteins such as cytokines, has been reported (albeit with a 45-min incubation period)<sup>52</sup>.

Labelling can also enhance the signals detected by fluidic mechanical biosensors. Gold nanoparticle labels have been used to seed additional gold precipitation, sufficiently enhancing their QCM mass signal to enable femtomolar detection of DNA<sup>48</sup>.

'Biobarcode' (BBA) sensors combine both amplification and nanoparticle labelling and have achieved record sensitivities of  $\sim 500$  aM (Fig. 1)<sup>72</sup>.

In general, it is complex to scale labelling and non-PCR amplification methods to highly multiplexed assays. Also, labelling and sandwich assays are inherently one-shot detection techniques — they are not readily adaptable to continuous, real-time monitoring. Furthermore, the most selective sandwich-type assays are predicated on the availability of two high-affinity capture agents, for example, antibodies. In this context, it is noteworthy that obtaining robust and effective capture agents is often a limiting factor in immunoassay development<sup>2</sup>.

**Diffusion, convection, reaction kinetics and response time.** Capture kinetics have a critical and underappreciated role in determining the overall sensor system performance. For most applications, a very fast flow rate is optimal for microfluidic devices — although this leads to a reduced percentage of captured target molecules, it increases the actual number of captured molecules per unit time. Although this might seem wasteful, the small volumes of microfluidic devices and their tiny maximal flow rates result in the use of very small sample aliquots — often in the range of microlitres, or less.

To illustrate these considerations we summarize the kinetics of analyte capture in a microfluidic channel. (See Box 1 and ref. 57). We define a critical length,  $L^* = 1.2 D^2 Q_V / (b_m^3 h_{\text{chan}}^2 k_{\text{on}}^3 w_{\text{chan}})$ , where  $D$  is diffusion rate,  $Q_V$  is flow rate,  $b_m$  is the number of receptor binding sites,  $h_{\text{chan}}$  is channel height,  $k_{\text{on}}$  is the rate of association and  $w_{\text{chan}}$  is channel width, over which analytes, owing to binding, become depleted near the functionalized surface to 50% of their initial (bulk) concentration. For sensors shorter than  $L^*$ , such depletion and, hence, mass transport itself, can safely be ignored. Conversely, for sensors significantly longer than  $L^*$ , depletion plays an increasingly important role. Figure 3 shows the strong dependence  $L^*$  has on  $k_{\text{on}}$  for a variety of microfluidic device geometries. For typical biological binding affinities — for example,  $k_{\text{on}} \sim 10^7 \text{ M}^{-1} \text{ s}^{-1}$ , characteristic of TNF binding to TNF-R1<sup>73</sup> —  $L^*$  ranges from micrometres to tens of millimetres depending on the flow geometry.

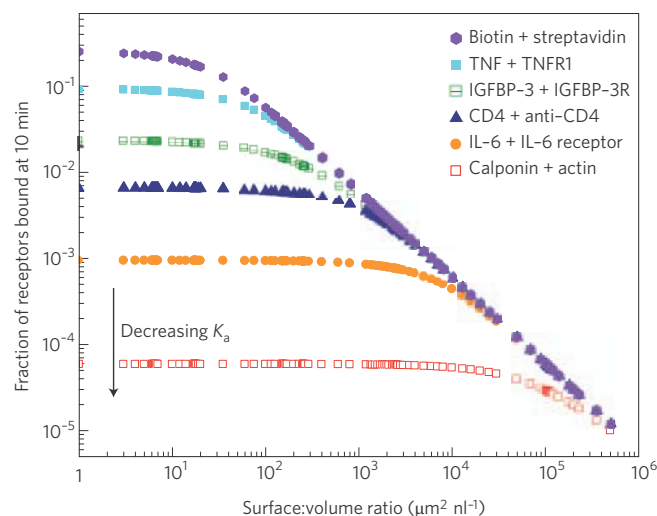


**Figure 4 | Effect of surface-area:volume ratio on bulk target depletion.**

The fraction of receptors bound at 10 min versus the surface-area:volume ratio for the six target-receptor pairs listed in Table 2 under reaction-limited conditions (Box 1): the affinity  $K_a$  of the pairs decreases from top to bottom. The fraction of bound receptors can be increased by reducing the surface-area:volume ratio. However, below a threshold (determined by  $K_a$ ), there is no further gain.

### Box 1 | Kinetics of microfluidic systems.

In microfluidic systems, it is essential to determine whether analytes are depleted near the active surfaces of sensors. Following Squires, Messinger and Manalis<sup>57</sup> we employ the Damkohler number,  $Da = (c_0 - \langle c_s \rangle) / \langle c_s \rangle$ , to characterize the importance of depletion at the surface, where  $c_0$  and  $\langle c_s \rangle$  are the bulk and average concentration at the device surface. For  $Da \ll 1$ , the kinetics of capture are entirely governed by reaction kinetics; for  $Da \gg 1$ , the kinetics become mass-transport limited. The Damkohler number can also be expressed as  $Da = k_{\text{on}} b_m A_{\text{sensor}} / (J / c_0)$ , where  $k_{\text{on}}$  is the rate of association,  $b_m$  the surface concentration of receptors on the sensor,  $A_{\text{sensor}}$  the surface area of the sensor, and  $J$  the flux of target molecules reaching the device through mass transport. This flux is given by<sup>57</sup>:

$$\begin{aligned} J &\sim D c_0 w_s Pe_H & Pe_H \ll 1 \\ J &\sim D c_0 w_s \pi (\ln(4/Pe_s^{1/2}) + 1.06)^{-1} & Pe_H \gg 1 \text{ and } Pe_s \ll 1 \\ J &\sim D c_0 w_s \pi (0.81 Pe_s^{1/3}) & Pe_H \gg 1 \text{ and } Pe_s \gg 1 \end{aligned}$$

where  $D$  is the diffusion rate,  $w_s$  is the sensor width,  $Pe_H \sim Q_V / D w_{\text{chan}}$  is the Peclet number with respect to the thickness of the microfluidic channel,  $h_{\text{chan}}$ ,  $Pe_s \sim 6(l_{\text{sensor}}/h_{\text{chan}})^2 Pe_H$  is the Peclet number with respect to the width of the channel,  $w_{\text{chan}}$ ,  $Q_V$  is the volumetric flow rate, and  $l_{\text{sensor}}$  is the sensor length in the direction of fluid flow. See ref. 57 for a more detailed discussion.

These expressions also allow us to estimate the time required to reach steady-state,  $\tau_{\text{ss}}$ . For the geometries and targets of Fig. 3,  $\tau_{\text{ss}}$  can range from seconds (for interactions with the lowest affinities) to hours.

**Concentration sensitivity versus absolute sensitivity.** For very small sample volumes, one may also need to consider depletion in the bulk solution. Table 2 summarizes the smallest volume at which the bulk concentration remains within 90% of the initial value at steady state. As microfluidic sample volumes are generally  $\sim \mu\text{l}$ , bulk depletion is often negligible. However, recent work on microfluidic single cell analysis exemplifies an important situation where depletion becomes relevant<sup>63</sup>: a sensitivity of  $\sim 2$  zeptomoles ( $10^{-20}$  moles or  $\sim 1,000$  copies) has been achieved by confining individual cells in a 5-nl chamber in which a bead-based immunofluorescence assay (IFA) was implemented. These are very small volumes compared with typical  $\sim \mu\text{l}$ -scale microfluidic assays. For reaction-limited systems (see Box 1), the time-dependent capture profile can be described by the expression,  $\delta b / \delta t = k_{\text{on}}(b_m - b(t))(c_0 - b(t)) / (V N_A)$ . Here  $b(t)$  is the number of target molecules bound to the surface at time,  $t$ ,  $V$  is the total (limited) volume of sample, and  $N_A$  is Avogadro's number. For detection at very low concentrations, we ignore terms of order  $(b(t)/b_m)^2$ . Figure 4 shows the fraction of receptors bound after 10 min in such an experiment for a range of target molecules and capture areas.

These considerations illustrate that nanoscale, and even microscale, sensors cannot capture sufficient targets from solution to become depletion-limited for most applications (Fig. 3). In cases where the analysis volume is extremely minute (for example, for the single-cell analyses mentioned previously), depletion can play a role for surface-to-volume ratios on the order of  $100 \mu\text{m}^2 \text{ nl}^{-1}$  or less (Fig. 4). Thus, for a sample volume  $\sim \text{nl}$ , significant gains in surface density of target molecules (and hence limits of detection) can be realized by scaling the active sensor surface to an area of roughly  $100 \mu\text{m}^2$ . Except for the highest affinity targets, further gains cannot be realized with smaller capture cross-sections (Fig. 4). The volumes at which depletion begins to play a role are summarized in Table 2 for several sensor geometries.



**Table 2 | Timescales for reaching biochemical steady state.**

Analyte(s)	$k_{\text{on}}$ ( $\text{M}^{-1}\text{s}^{-1}$ )	$K_{\text{a}}$ ( $\text{M}^{-1}$ )	$Q_{\text{v}}=130\mu\text{lmin}^{-1}$ $t_{\text{chan}}=60\mu\text{m}$ $w_{\text{chan}}=100\mu\text{m}$		$Q_{\text{v}}=20\mu\text{lmin}^{-1}$ $t_{\text{chan}}=10\mu\text{m}$ $w_{\text{chan}}=70\mu\text{m}$		$Q_{\text{v}}=74\text{nllmin}^{-1}$ $t_{\text{chan}}=3\mu\text{m}$ $w_{\text{chan}}=8\mu\text{m}$		$Q_{\text{v}}=0.47\text{nl min}^{-1}$ $t_{\text{chan}}=700\text{nm}$ $w_{\text{chan}}=4\mu\text{m}$		
			Equil. time (min)	Volume (10% bound)	Volume (10% bound)	Volume (10% bound)	Volume (10% bound)	Volume (10% bound)			
$L_{\text{sensor}}$			10 $\mu\text{m}$	200 $\mu\text{m}$	10 $\mu\text{m}$	200 $\mu\text{m}$	10 $\mu\text{m}$	200 $\mu\text{m}$	10 $\mu\text{m}$	200 $\mu\text{m}$	
Analyte											
Calponin + actin	$1\times10^7$	$6\times10^7$	0.1	5 pl	98 pl	3 pl	68 pl	0.4 pl	7.8 pl	0.2 pl	3.9 pl
IL-6+IL-6R	$2\times10^5$	$2.4\times10^8$	20	0.2 nl	4 nl	0.1nl	2.8 nl	16 pl	0.3nl	8 pl	0.2 nl
IGFBP-3 +IGFBP-3R	$1.4\times10^7$	$2.6\times10^9$	3	2 nl	40 nl	1nl	28 nl	0.2 nl	3.2 nl	80 pl	1.6 nl
CD4 + anti-CD4R	$1.2\times10^6$	$4.1\times10^9$	55	3 nl	66 nl	2 nl	47 nl	0.3 nl	5.3 nl	0.1nl	2.7 nl
TNF + TNFR1	$1.8\times10^7$	$5.3\times10^{10}$	32	29 nl	0.6 $\mu\text{l}$	20 nl	0.4 $\mu\text{l}$	2 nl	46 nl	1 nl	23 nl
Biotin + streptavidin	$5\times10^7$	$2.9\times10^{13}$	33	83 nl	2 $\mu\text{l}$	58 nl	1.2 $\mu\text{l}$	7 nl	0.1 $\mu\text{l}$	3 nl	66 nl

An important goal for many microfluidic-embedded sensors is achieving 'fast detection'. Here we provide estimates of the equilibration time,  $\tau_{\text{eq}}$ , for six analytes (in order of increasing affinity  $K_{\text{a}}$ ) for detection at a concentration of 10 pM for two sensor lengths (10  $\mu\text{m}$  and 200  $\mu\text{m}$ ) and four different microfluidic geometries (in order of decreasing flow rate and channel cross-section). For all but the highest affinity analyte (biotin + streptavidin), all the devices are reaction limited at these flow rates and  $\tau_{\text{eq}} = K_{\text{a}}/(k_{\text{on}}(1 + c_{\text{c}}K_{\text{a}}))$ ; in other words  $\tau_{\text{eq}}$  does not depend on the sensor length or microfluidic geometry. For biotin + streptavidin,  $\tau_{\text{eq}}$  increases from 33 min (length = 10  $\mu\text{m}$ ; flow = 130  $\mu\text{lmin}^{-1}$ ; channel cross-section =  $60\mu\text{m} \times 100\mu\text{m}$ ) to 55 min (length = 200  $\mu\text{m}$ ; flow = 0.47  $\text{nllmin}^{-1}$ ; channel cross-section =  $700\text{nm} \times 4\mu\text{m}$ ;  $\tau_{\text{eq}}$  not shown in Table) as the system changes from being reaction limited to transport limited. We also provide examples of the sample volumes below which more than 10% of the analyte molecules are bound to the device in equilibrium and bulk depletion must be considered (see main text and Fig. 4). Above these volumes only surface depletion need be considered (Fig. 3), and analyte can be recirculated without degradation of performance. For all cases, we assume that the sensor width is half the channel width and that its thickness is negligible. The flow rates  $Q_{\text{v}}$  were chosen under the assumption that the channel has the dimensions listed above over a length of 500  $\mu\text{m}$ , and that it is in series with a channel with  $t_{\text{chan}} = 2\text{cm}$ ;  $t_{\text{chan}} = 60\mu\text{m}$  and  $w_{\text{chan}} = 100\mu\text{m}$  (included to represent the region of the microfluidic channel in which sample processing would occur). The channel is presumed to be pressurized to 5 psi.

## Force and energy sensing

Mechanical devices can perform other types of sensing, especially molecular-force and energy-based sensing. The ability to access other modes of operation highlights the potential of new sensors to open different avenues of fundamental biological research, and to enable applications beyond the simple 'on/off' indication of target analyte capture.

Chemically functionalized atomic force microscopes have been employed to measure the force of intramolecular interactions<sup>74–78</sup>, arrays of polydimethylsiloxane (PDMS) posts have been used to measure forces exerted by cells<sup>79</sup>, and optical tweezers have been used to measure the elasticity of cells and have measured significant (three-fold) differences in deformability between cancerous and normal cells<sup>80,81</sup>. Measurement of forces, elasticity and displacement is ideally suited to the mechanical domain and, in particular, the unprecedented sensitivity of nanoelectromechanical systems (NEMS) devices. Many of these applications are just beginning to be explored — a recent example is the use of surface-stress sensors to measure conformational changes of proteins<sup>12</sup> and DNA<sup>13</sup>. In the energy domain, microfluidic calorimeters with potential for resolving the metabolic output of individual cells are on the horizon<sup>82</sup>. Here we highlight several of these promising new areas of research.

**Fluid-based force sensing.** The atomic force microscope (AFM) is best known for probing various systems with atomic resolution in vacuum, but it can also image samples at atmospheric pressure and immersed in fluid. Measurement of the elastic properties of live cells has also been demonstrated<sup>83</sup>. As with mass sensitivity, improvements in force resolution are achieved by reducing the dimensions of the sensor (Fig. 5). Current microcantilevers have the sensitivity to resolve forces at the level of individual hydrogen bonds and to investigate biological molecules based on their force-extension profile as the molecule is stretched<sup>84,77,78</sup> or ruptured<sup>74</sup>. Bond lifetime and dynamic force spectroscopy experiments have enabled measurements of bond formation and dissociation at the single-molecule level, yielding new insights to molecular behaviour, binding states and reaction pathways. In particular, unbinding force measurements have been used to study receptor–ligand dissociation rates,  $k_{\text{off}}$ <sup>75,85</sup>. However, care must be taken in interpreting these rates, as the initial 'bound state' and hence the measured rupture force, is strongly dependent on its history<sup>86</sup>. With careful study, significant information on the energy landscape for

receptor–ligand bonds can be obtained, yielding good agreement between simulations<sup>87</sup> and experiments<sup>76</sup>.

Of particular interest in this domain have been studies of cell adhesion and the interaction between mechanical stimuli and chemical circuitry in the cell<sup>88</sup>. Single-molecule atomic force microscopy techniques, in which the bonds are stretched but not ruptured, have allowed studies of the dynamic rearrangement of the active site of an enzyme during catalysis<sup>77</sup>, and have also been used to investigate protein<sup>78,84</sup> and RNA<sup>89</sup> folding. In single-cell force spectroscopy, a cell is attached to an AFM cantilever and brought into contact with a substrate at a predetermined contact force, kept stationary for a fixed time, and then pulled away from the substrate. Individual bond-breaking events can be resolved, enabling the investigation of adhesion forces — down to the level of individual receptor interactions. This has been used to investigate a wide variety of phenomena, from the properties of cell adhesion itself<sup>90</sup>, to force interaction in cancer<sup>91</sup> and immune response<sup>92</sup>. Most recently, functionalized surfaces have been used to investigate receptor crosstalk<sup>93</sup>.

**Fluid-based energy sensing devices.** The inherently small heat capacities of suspended nanoscale devices make them ideal candidates for ultrasensitive calorimetry. Indeed, vacuum-based nanoscale devices have achieved a resolution of 0.5 aJ K<sup>−1</sup> at 2 K (ref. 94). Scaling these chip calorimeters up to room temperature operation, and embedding them in integrated microfluidics, offers the prospect of high-throughput measurements requiring very low sample consumption. In particular, a power sensitivity on the order of nanowatts, on sample volumes of a few nanolitres, has been achieved<sup>82</sup>. Next-generation improvements on the horizon suggest that sensitivities on the scale of picowatts are feasible; this will enable metabolic measurements at the level of individual cells.

## Practical aspects of fluidic mechanical biosensors

A major challenge for all NEMS devices has been development of efficient actuation and transduction methods. Here we provide a brief overview of common techniques and describe recent advances (see ref. 95 for a comprehensive discussion).

Optical detection, a cornerstone of microelectromechanical devices such as AFM probes, becomes increasingly challenging to implement as the device dimensions scale below an optical wavelength. Nevertheless, devices with widths as small as 50 nm have



been measured optically through the use of optical interferometry. Measurements have been performed both on individual devices<sup>96,97</sup> and on grating-based systems<sup>98</sup>. Recently, near-field, non-interferometric optical transduction has been identified as a promising alternative for arrays of nanocantilevers<sup>99</sup>. The latter holds significant potential for co-integration with on-chip light sources, because non-interferometric techniques do not require a coherent light source. Evanescent coupling to the substrate of a propagating light field has also been used to drive NEMS<sup>100</sup>.

Electrostatic detection and actuation, used ubiquitously in integrated microelectromechanical systems (MEMS), generally lose efficiency for nanoscale devices. Capacitance scales as area/separation but practical limits on drive-gate gaps ultimately limit reduction of their dimensions. Given the higher frequencies of NEMS compared with MEMS, a large fraction of the electrostatically based drive and detection signals are lost through parasitic capacitances. However, with an appropriate LC network for

impedance transformation it is possible, on resonance, to couple electrostatically through a gate electrode to the device with reasonable efficiency. This technique has been used to measure a NEMS array with closely spaced resonance frequencies (above 10 MHz) using a single RF circuit (Fig. 6a,b)<sup>101</sup>.

Thermoelastic actuation has been demonstrated — through photothermal heating in air<sup>102</sup> and liquid<sup>103</sup>, and through integrated electrothermal heating in both air<sup>104</sup> and liquid<sup>105</sup>. The thermally induced elastic strain, a measure of stored energy density, is generally constant as the device dimensions are uniformly scaled down. This makes thermoelastic actuation promising for increasingly smaller NEMS devices.

Piezoelectric actuation has also been used extensively for MEMS devices in both air<sup>106</sup> and liquid<sup>30</sup>. Advances in the quality of piezoelectric ultra-thin film (< 20 nm) materials have recently enabled their application to NEMS<sup>107</sup>. An important benefit of piezoelectric actuation is its exceptionally small power consumption,

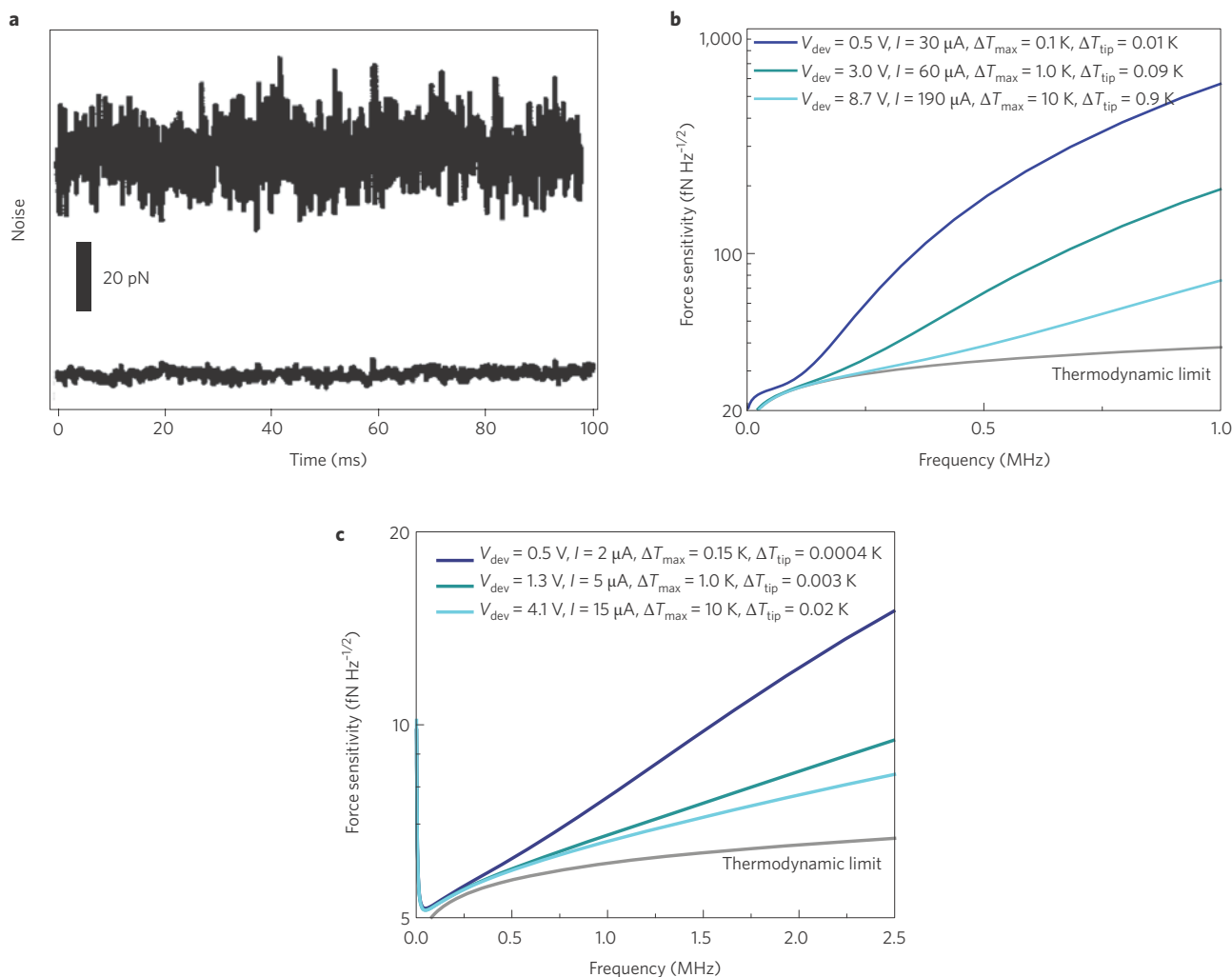


**Figure 5 | Fluidic nanomechanical biosensors.** Demonstration of reduction in force noise through the overall reduction of cantilever dimensions. **a**, Noise versus time for a large cantilever (length = 200 μm; spring constant  $k = 0.060 \text{ N m}^{-1}$ ; top trace) and a small cantilever (length = 10 μm;  $k = 0.060 \text{ N m}^{-1}$ ; bottom trace)<sup>131</sup>. **b**, Theoretical predictions for total force sensitivity (including thermomechanical Brownian noise, Johnson noise and typical readout amplifier noise) on a logarithmic scale versus frequency for a silicon piezoresistive cantilever immersed in water and operating at room temperature for three different sets of conditions; the thermodynamic limit (that is, just Brownian noise) is also shown for reference. The sensitivity depends on the maximum tolerable temperature rise both at the tip  $\Delta T_{\text{tip}}$  and the position of maximum heating  $\Delta T_{\text{max}}$ . As the bias voltage  $V_{\text{dev}}$  and bias current  $I$  increase, both  $\Delta T_{\text{tip}}$  and  $\Delta T_{\text{max}}$  also increase, and the sensitivity improves, approaching the thermodynamic limit. The cantilever device dimensions are:  $t = 130 \text{ nm}$ ,  $w = 2.5 \text{ μm}$ ,  $l = 15 \text{ μm}$ . **c**, Analogous plot to **b** for a smaller cantilever<sup>132</sup> showing qualitatively similar behaviour but substantially higher sensitivity (note that the scale on the y-axis is different):  $t = 30 \text{ nm}$ ,  $w = 100 \text{ nm}$ ,  $l = 3 \text{ μm}$ . At frequencies below 1 MHz, the system approaches the thermodynamic limit, and the sensitivity remains within about 20% of the fluidic noise floor at the relatively low bias voltage of 0.5 V. Below 0.25 MHz, the total sensitivity is  $\sim 5 \text{ fN } \sqrt{\text{Hz}^{-1}}$  (for reasonable bias voltages). Figure reproduced with permission from: **a**, ref. 131, © 1999 AIP; **b,c**, ref. 132, © 2007 Springer.

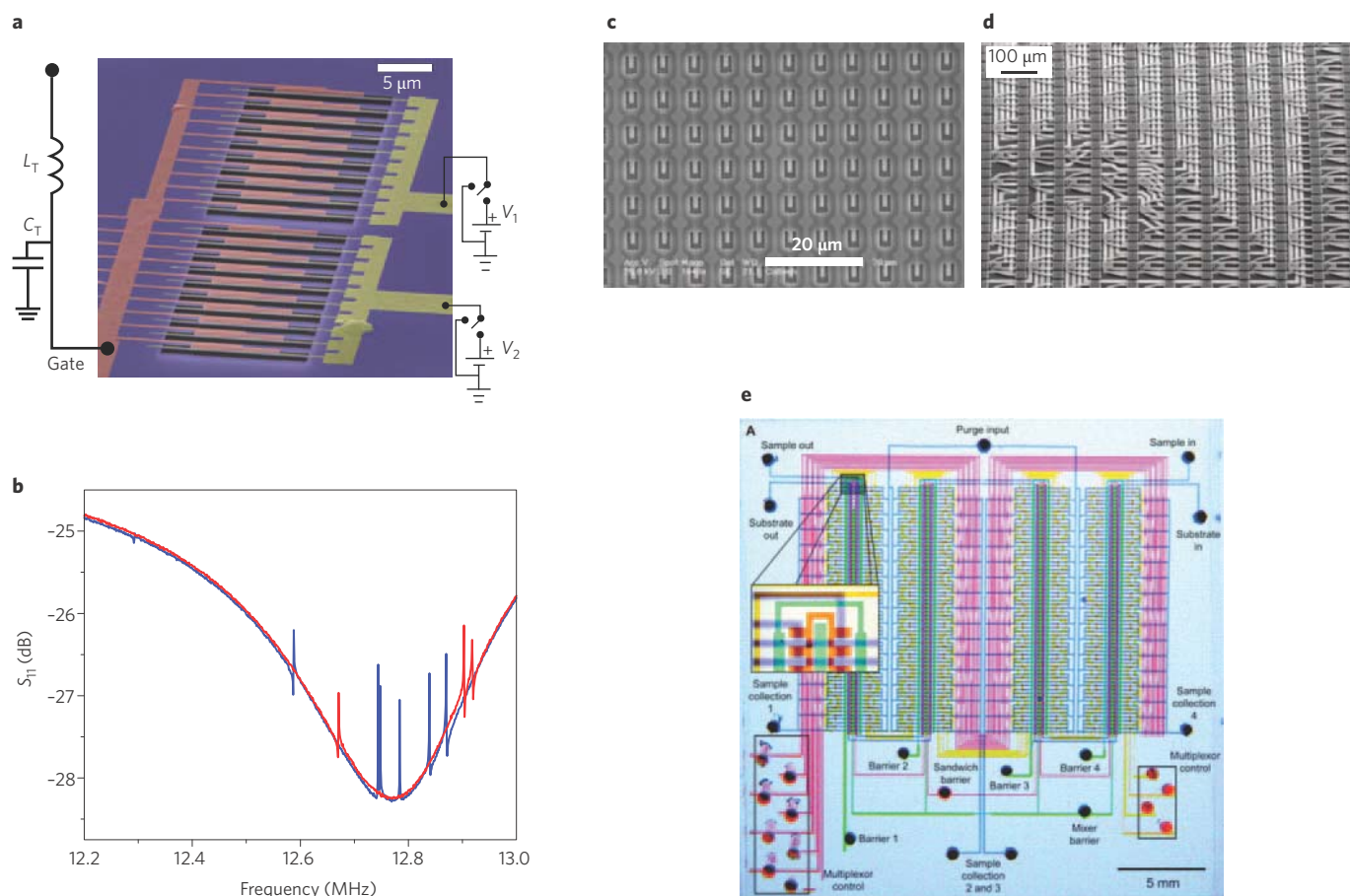


**Figure 6 | NEMS arrays and system integration.** **a**, False-colour SEM image of an array of 20 silicon nitride nanomechanical resonators (in two separately biased banks) with capacitive readout and actuation<sup>101</sup>; the resonant frequencies of the resonators are ~12 MHz. **b**, Resonance spectrum (oscillation amplitude ( $S_{11}$ ) versus frequency) of the array in **a**. It is possible to read out the array with a single radiofrequency readout circuit<sup>101</sup>. Seven resonators in bank 1 (blue trace) and three resonators in bank 2 (red trace) were detected in this frequency range. **c**, Array of silicon cantilevers: each cantilever is 2.8- $\mu\text{m}$  long and 0.7- $\mu\text{m}$  wide, with the 'legs' being 200-nm wide. A piezoresistive approach was used for readout. Image courtesy of P. Andreucci (Minatec, Leti, CEA). **d**, SEM of a section of a 4,096 silicon cantilever array, transferred onto a wiring wafer. The transfer is done on the 100-mm wafer scale, with approximately 50 such arrays per wafer<sup>114</sup>. These cantilevers were designed for memory storage applications, with resistors at the base to induce (the write step) and measure (read step) the deflection. **e**, Multiplexed microfluidics. PDMS microvalves enable independent compartmentalization, purging and pairwise mixing for each of the 256 chambers on the chip<sup>115</sup>. Figure reproduced with permission from: **a, b**, ref. 101, © 2007 ACS; **d**, ref. 114, © 2004 IEEE; **e**, ref. 115, © 2002 AAAS.

owing to the minimal current flow through the device — especially compared with that of thermoelastic actuation. As the piezoelectric effect itself generates voltages when the NEMS vibrates, it can be used for detection as well as actuation. As with capacitive detection, however, direct signal transduction faces the challenge of relatively small-magnitude, high-frequency signals originating from high-source impedances, in the presence of substantial parasitic capacitances.

Piezoresistive detection technique is now widely used for room temperature NEMS applications. Devices with doped semiconductor piezoresistive sensors have a long history in MEMS<sup>108–110</sup>. However, the use of these materials in nanoscale devices is challenging because the doped layer must remain thin compared with the total device thickness. Requisite structures at nanoscale dimensions also require exceptionally careful processing to avoid damage to the ultrathin doped surface layer required. The displacement transducers that result suffer from high Johnson noise given their relatively high impedance, and from very high  $1/f$  noise owing to their low carrier concentrations and small volumes<sup>111</sup>. Recent work shows these difficulties become exacerbated with semiconducting transducers as their size is scaled downwards, but can be overcome through the use of metallic piezoresistors<sup>112</sup>.

### Future nanosystems for complex biosensing

The ultimate mechanical biosensing systems will combine precise microfluidic sample handling, automated and complex preparatory protocols, and highly sensitive nanomechanical sensing elements in multiplexed device arrays that can be readily mass-producible by microelectronic fabrication technologies. Although most results published so far describe measurements from one or, at most, a few biosensors, it has already been shown that thousands of suspended cantilevers can be fabricated to fit on a chip measuring a few millimetres by a few millimetres (Fig. 6c). The outstanding challenges, therefore, are the difficulty of differentially functionalizing closely packed sensors (which is a front-end issue) and the complexity of multiplexing the electrical readout of a dense array of devices (which is a back-end issue).

Effort is at present focused on leveraging the existing infrastructure for the very large-scale integration of silicon microelectronics (that is, complementary metal oxide semiconductor (CMOS) devices) to facilitate the very large-scale integration of NEMS. Routes being taken include development of a unified, monolithic NEMS-CMOS process<sup>113</sup> and a multilayer, multichip, three-dimensional stacking or hybridization process for NEMS and CMOS<sup>114</sup>.

The IBM Millipede project demonstrates that wafer-level transfer of MEMS devices to the surface of other wafers is both achievable and robust. This project has achieved device densities  $\sim 100$  cantilevers  $\text{mm}^{-2}$  and interconnect densities  $\sim 300$   $\text{mm}^{-2}$  (Fig. 6d; ref. 114). Highly multiplexed microfluidics have also been demonstrated (Fig. 6e)<sup>115</sup> and are leading to a growing range of applications<sup>116,117</sup>. The outstanding task is the integration of complex microfluidics and dense arrays of nanoscale biosensors.

In terms of performance for diagnostic applications, we have already discussed examples where mechanical biosensors have reached the stage where non-specific binding and other factors such as sensor drift — rather than the inherent device mass sensitivity — set the limit of detection. For applications involving the detection of rare biomarkers in serum, enhancing the limits of detection requires confronting the problem that the concentrations of the most abundant proteins in samples are many orders of magnitude higher than those of the least abundant targets. Pre-concentration and/or immunoaffinity depletion can help to some extent, but the ultimate efficacy of such approaches is compromised by the tendency for competing molecules to be concentrated along with the target of interest and/or for the target to be depleted along with the competing molecules.

Another problem is that small, low-abundance target proteins (such as cytokines) can be sequestered by proteins that are abundant in serum (such as albumin). Indeed it has been shown that sequestered biomarkers may exist at concentrations that are 10–500 times greater than that of their free counterparts<sup>118</sup>. Standard procedures for the depletion of albumin can lead to significant depletion of cytokine<sup>119</sup>. Effective solutions to these issues will probably transcend the simplest of label-free approaches — and involve slower, complex and multi-step protocols such as high-affinity sandwich assays. For laboratory applications such as rapid, high-throughput drug screening, however, it may be possible to work with reasonably pure solutions where the range of concentrations is smaller. For such cases, there will always be significant benefit to improving the device sensitivity.

We have seen how microfluidic technology provides researchers with the capability to place individual cells in chambers with picolitre to nanolitre scale volumes<sup>117,120</sup>. This circumvents the massive dilution of samples that is inherent to conventional approaches and can therefore maintain proteins obtained from individual cells — be it by secretion or cell lysis — at concentrations that are readily detected with the most sensitive technologies, represented in Fig. 1. Although secretion rates from individual cells are highly variable, and depend on the specific molecules secreted, detection on the picomolar scale serves as an important initial benchmark. We illustrate this with the example of native (unstimulated) human monomyeloid cells, which secrete an average rate of  $\sim 7,000$  TNF- $\alpha$  molecules per minute per cell<sup>121</sup>. For an individual cell sequestered in a volume of 1 nL, this would correspond to a concentration increase of 40 fM  $\text{min}^{-1}$ , and this rate can be increased by a factor of  $\sim 80$  if the cells are stimulated. The levels of detector performance needed to measure these processes are included in Fig. 1 as an example of an application that requires sensitivity beyond that needed for many diagnostic assays.

Single-cell analyses also have the potential to improve our understanding of cellular heterogeneity by exploring in detail variations in the responses of genetically identical cells to identical stimuli<sup>63,117</sup>. No existing technology can perform simultaneous, real-time, quantitative assays on large populations (arrays) of individual cells, but Fig. 1 makes it evident that micro- and nanoscale sensors may soon make this feasible.

Critical to achieving such goals is development of new methods for functionalization, especially approaches enabling proximal multiplexing. For example, Huber *et al.* have demonstrated simultaneous protein and DNA detection in a single microcantilever surface-stress sensor array<sup>122</sup>. Detection of numerous DNA<sup>123</sup> and protein<sup>124</sup> targets has also been demonstrated. However, existing approaches typically

employ methods (such as functionalization in separate microcapillaries<sup>123</sup> or ink-jet spotting,<sup>4,125</sup>) that cannot be reduced in size to nanoscale dimensions or scaled upwards to make large, multiplexed arrays with, say, thousands of elements. Photolabile crosslinkers and photolithographic light-directed synthesis, as in gene chips and release protocols<sup>57</sup>, show promise for the functionalization of arrays of devices, but the diffraction limit makes it difficult to scale this approach down to the nanoscale. More elaborate techniques, such as scanning-probe-based coating deposition<sup>126</sup> or localized electrochemical growth<sup>127</sup>, may prove helpful.

Many challenges remain — from the development of better capture agents (see ref. 2 for a review) to the integration of arrays of advanced nanosensors with conventional microelectronic fabrication techniques — but the ultimate goal of developing tools that are capable of high-throughput studies of biological systems at the level of single cells and individual molecules will continue to drive the field forwards.

## References

- Braun, T. *et al.* Quantitative time-resolved measurement of membrane protein-ligand interactions using microcantilever array sensors. *Nature Nanotech.* **4**, 179–185 (2009).
- Phelan, M. L. & Nock, S. Generation of bioreagents for protein chips. *Proteomics* **3**, 2123–2134 (2003).
- von Muhlen, M. G., Brault, N. D., Knudsen, S. M., Jiang, S. & Manalis, S. R. Label-free biomarker sensing in undiluted serum with suspended microchannel resonators. *Anal. Chem.* **82**, 1905–1910 (2010).  
**This work is notable for the high sensitivity (300 pM) and fast response time ( $\sim 1$  min).**
- Backmann, N. *et al.* A label-free immunosensor array using single-chain antibody fragments. *Proc. Natl Acad. Sci. USA* **102**, 14587–14952 (2005).  
**The authors use a microcantilever with static-mode deflection to achieve a sensitivity of  $\approx 1$  nM, and include a detailed discussion of device functionalization.**
- Waggoner, P. S., Varshney, M. & Craighead, H. G. Detection of prostate specific antigen with nanomechanical resonators. *Lab Chip* **9**, 3095–3099 (2009).  
**The authors report femtomolar detection from serum through fluid phase capture and detection *in vacuo*.**
- Ibach, H. The role of surface stress in reconstruction, epitaxial growth and stabilization of mesoscopic structures. *Surf. Sci.* **29**, 193–263 (1997).
- Wu, G. *et al.* Bioassay of prostate-specific antigen (PSA) using microcantilevers. *Nature Biotechnol.* **19**, 856–860 (2001).
- Fritz, J. *et al.* Translating biomolecular recognition into nanomechanics. *Science* **288**, 316–318 (2000).
- Mertens, J. *et al.* Label-free detection of DNA hybridization based on hydration-induced tension in nucleic acid films. *Nature Nanotech.* **3**, 302–307 (2008).
- Zhang, J. *et al.* Rapid and label-free nanomechanical detection of biomarker transcripts in human RNA. *Nature Nanotech.* **1**, 214–220 (2006).
- Ndieyira, J. W. *et al.* Nanomechanical detection of antibiotic-mucopeptide binding in a model for superbug drug resistance. *Nature Nanotech.* **3**, 691–696 (2008).
- Braun, T. *et al.* Conformational change of bacteriorhodopsin quantitatively monitored by microcantilever sensors. *Biophys. J.* **90**, 2970–2977 (2006).
- Shu, W. *et al.* DNA molecular motor driven micromechanical cantilever arrays. *J. Am. Chem. Soc.* **127**, 17054–17060 (2005).
- Wee, K. W. *et al.* Novel electrical detection of label-free disease marker proteins using piezoresistive self-sensing micro-cantilevers. *Biosens. Bioelectron.* **20**, 1932–1938 (2005).
- Rasmussen, P. A., Thaysen, J., Hansen, O., Eriksen, S. C. & Boisen, A., Optimised cantilever biosensor with piezoresistive read-out. *Ultramicroscopy* **97**, 371–376 (2003).
- Stoney, G. G. The tension of metallic films deposited by electrolysis. *Proc. R. Soc. Lond. A* **82**, 172–175 (1909).
- Sader, J. E. Surface stress induced deflections of cantilever plates with applications to the atomic force microscopy: Rectangular plates. *J. Appl. Phys.* **89**, 2911–2921 (2001).
- Gfeller, K. Y., Nugaeva, N. & Hegner, M. Micromechanical oscillators as rapid biosensor for the detection of active growth of *Escherichia coli*. *Biosens. Bioelectron.* **21**, 528–533 (2005).
- Gfeller, K. Y., Nugaeva, N. & Hegner, M. Rapid biosensor for detection of antibiotic-selective growth of *Escherichia coli*. *Appl. Environ. Microbiol.* **71**, 2626–2631 (2005).  
**The growth and detection of *E. coli* was performed using dynamic mode microcantilevers: the sensitivity was  $\sim 100$  cells and the detection times were less than one hour.**



20. Yang, Y. T., Callegari, C., Feng, X. L., Ekinci, K. L. & Roukes, M. L. Zeptogram-scale nanomechanical mass sensing. *Nano Lett.* **6**, 583–586 (2006).
21. Jensen, K., Kim, K. & Zettl, A. An atomic-resolution nanomechanical mass sensor. *Nature Nanotech.* **3**, 533–537 (2008).
22. Gupta, A., Akin, D. & Bashir, R. Single virus particle mass detection using microresonators with nanoscale thickness. *Appl. Phys. Lett.* **84**, 1976–1978 (2004).
23. Ilic, B., Yang, Y. & Craighead, H. G. Virus detection using nanoelectromechanical devices. *Appl. Phys. Lett.* **85**, 2604–2606 (2004).
24. Park, K. *et al.* Measurement of adherent cell mass and growth. *Proc. Natl Acad. Sci. USA* **107**, 20691–20696 (2010).
25. Park, K. *et al.* Concentration, growth and mass measurements of mammalian cells on silicon cantilevers. *Lab Chip* **8**, 1034–1041 (2008).
26. Sader, J. E. Frequency response of cantilever beams immersed in viscous fluids with applications to the atomic force microscope. *J. Appl. Phys.* **84**, 64–76 (1998).
27. Van Eysden, C. A. & Sader, J. E. Frequency response of cantilever beams immersed in viscous fluids with applications to the atomic force microscope: Arbitrary mode order. *J. Appl. Phys.* **101**, 044908 (2007).
- This paper includes a detailed theoretical analysis of the viscous damping of fluid-immersed cantilevers.**
28. Braun, T. *et al.* Micromechanical mass sensors for biomolecular detection in a physiological environment. *Phys. Rev. E* **72**, 031907 (2005).
- The authors use dynamic mode mass detection with microcantilevers to achieve a resolution of 7 ng.**
29. Ghatkesar, M. K. *et al.* Higher modes of vibration increase mass sensitivity in nanomechanical microcantilevers. *Nanotechnology* **18**, 445502 (2007).
30. Hwang, K. S. *et al.* In-situ quantitative analysis of a prostate-specific antigen (PSA) using a nanomechanical PZT cantilever. *Lab Chip* **4**, 547–552 (2004).
31. Lee, J. H., Kim, T. S. & Yoon, K. H. Effect of mass and stress on resonant frequency shift of functionalized Pb(Zr<sub>0.52</sub>Ti<sub>0.48</sub>)O<sub>3</sub> thin film microcantilever for the detection of C-reactive protein. *Appl. Phys. Lett.* **84**, 3187–3189 (2004).
32. McFarland, A. W., Poggi, M. A., Doyle, M. J., Bottomley, L. A. & Colton, J. S. Influence of surface stress on the resonance behavior of microcantilevers. *Appl. Phys. Lett.* **87**, 053505 (2005).
33. Lu, P., Lee, H. P., Lu, C. & O'Shea, S. J. Surface stress effects on the resonance properties of cantilever sensors. *Phys. Rev. B* **72**, 085405 (2005).
34. Lachut, M. J. & Sader, J. E. Effect of surface stress on the stiffness of cantilever plates. *Phys. Rev. Lett.* **99**, 206102 (2007).
35. Tamayo, J., Ramos, D., Mertens, J. & Calleja, M. Effect of the adsorbate stiffness on the resonance response of microcantilever sensors. *Appl. Phys. Lett.* **89**, 224104 (2006).
36. Gupta, A. K. *et al.* Anomalous resonance in a nanomechanical biosensor. *Proc. Natl Acad. Sci. USA* **103**, 13362–13367 (2006).
37. Burg, T. P. *et al.* Weighing of biomolecules, single cells and single nanoparticles in fluid. *Nature* **446**, 1066–1069 (2007).
38. Barton, R. A. *et al.* Fabrication of a nanomechanical mass sensor containing a nanofluidic channel. *Nano Lett.* **10**, 2058–2063 (2010).
39. Zuniga, C., Rinaldi, M. & Piazza, G. High frequency piezoelectric resonant nanochannels for bio-sensing applications in liquid environment. *IEEE Sensors* **2010** 52–55 (November 2010).
40. Burg, T. P., Sader, J. E. & Manalis, S. R. Nonmonotonic energy dissipation in microfluidic resonators. *Phys. Rev. Lett.* **102**, 228103 (2009).
41. Sader, J. E., Burg, T. P. & Manalis, S. R. Energy dissipation in microfluidic beam resonators. *J. Fluid. Mech.* **650**, 215–250 (2010).
42. Bryan, A. K., Goranov, A., Amon, A. & Manalis, S. R. Measurement of mass, density, and volume during the cell cycle of yeast. *Proc. Natl Acad. Sci. USA* **107**, 999–1004 (2010).
43. Godin, M. *et al.* Using buoyant mass to measure the growth of single cells. *Nature Methods* **7**, 387–390 (2010).
44. Knudsen, S. M., von Muhlen, M. G., Schauer, D. B. & Manalis, S. R. Determination of bacterial antibiotic resistance based on osmotic shock response. *Anal. Chem.* **81**, 7087–7090 (2009).
45. Arlett, J. L. & Roukes, M. L. Ultimate sensitivity limits for mass sensing with hollow micro/nanochannel resonators. *J. Appl. Phys.* **108**, 084701 (2010).
46. Kim, N., Kim, D.-K. & Cho, Y.-J. Development of indirect-competitive quartz crystal microbalance immunosensor for C-reactive protein. *Sensor. Actuat. B-Chem.* **143**, 444–448 (2009).
47. Kurosawa, S. *et al.* Evaluation of a high-affinity QCM immunosensor using antibody fragmentation and 2-methacryloyloxyethyl phosphorylcholine (MPC) polymer. *Biosens. Bioelectron.* **20**, 1134–1139 (2004).
48. Weizmann, Y., Patolsky, F. & Willner, I. Amplified detection of DNA and analysis of single-base mismatches by the catalyzed deposition of gold on Au-nanoparticles. *Analyst* **126**, 1502–1504 (2001).
49. Armani, A. M., Kulkarni, R. P., Fraser, S. E., Flagan, R. C. & Vahala, K. J. Label-free, single-molecule detection with optical microcavities. *Science* **314**, 783–787 (2007).
50. Arnold, S., Shopova, S. I. & Holler, S. Whispering gallery mode bio-sensor for label-free detection of single molecules: thermo-optic vs. reactive mechanism. *Opt. Express* **18**, 281–287 (2010).
51. Washburn, A. L., Luchansky, M. S., Bowman, A. L. & Bailey, R. C. Quantitative, label-free detection of five protein biomarkers using multiplexed arrays of silicon photonic microring resonators. *Anal. Chem.* **82**, 69–72 (2010).
- The authors report quantitative, parallel detection from five protein mixtures.**
52. Luchansky, M. S. & Bailey, R. C. Silicon photonic microring resonators for quantitative cytokine detection and T-cell secretion analysis. *Anal. Chem.* **82**, 1975–1981 (2010).
53. Stern, E. *et al.* Label-free immunodetection with CMOS-compatible semiconducting nanowires. *Nature* **445**, 519–522 (2007).
54. Zheng, G., Gao, X. P. A. & Lieber, C. M. Frequency domain detection of biomolecules using silicon nanowire biosensors. *Nano Lett.* **10**, 3179–3183 (2010).
55. Bunimovich, Y. L. *et al.* Quantitative real-time measurement of DNA hybridization with alkylated nonoxidized silicon nanowires in electrolyte solution. *J. Am. Chem. Soc.* **128**, 16323–16331 (2006).
56. Gao, X. P. A., Zheng, G. & Lieber, C. M. Subthreshold regime has the optimal sensitivity for nanowire FET biosensors. *Nano Lett.* **10**, 547–552 (2010).
57. Squires, T. M., Messinger, R. J. & Manalis, S. R. Making it stick: Convection reaction and diffusion in surface-based biosensors. *Nature. Biotechnol.* **26**, 417–426 (2008).
- This review article contains a detailed kinetics analysis that is relevant to all biosensors.**
58. Rich, R. & Mysza, D. G. Advances in surface plasmon resonance biosensor analysis. *Curr. Opin. Biotechnol.* **11**, 54–61 (2000).
59. Skivesen, N. *et al.* Photonic-crystal waveguide biosensor. *Opt. Express* **15**, 3169–3176 (2007).
60. Yao, X. *et al.* Sub-attomole oligonucleotide and p53 cDNA determinations via a high-resolution surface plasmon resonance combined with oligonucleotide-capped gold nanoparticle signal amplification. *Anal. Biochem.* **354**, 220–228 (2006).
61. Cesaro-Tadic, S. *et al.* High-sensitivity miniaturized immunoassays for tumor necrosis factor  $\alpha$  using microfluidic systems. *Lab Chip* **4**, 563–569 (2004).
62. Fan, R. *et al.* Integrated barcode chips for rapid, multiplexed analysis of proteins in microliter quantities of blood. *Nature Biotechnol.* **26**, 1373–1378 (2008).
63. Diercks, A. H. *et al.* A microfluidic device for multiplexed protein detection in nano-liter volumes. *Anal. Biochem.* **386**, 30–35 (2009).
64. Harris, R. & Lohr, K. N. Screening for Prostate Cancer: An Update of the Evidence for the U. S. Preventive Services Task Force. *Ann. Intern. Med.* **137**, 915–916 (2002). See also: [http://en.wikipedia.org/wiki/Prostate\\_specific\\_antigen](http://en.wikipedia.org/wiki/Prostate_specific_antigen)
65. Carrano, J. *Chemical and Biological Sensor Standards Study* (DARPA, 2005). Available at <http://go.nature.com/JNBVGN>
66. Steward, C. C. & Steward, S. J. In *Cytometry* 3rd edn, Vol. 63 (ed. Darzynkiewicz, Z.) 223 (2001).
67. Konopka, K. & Neilands, J. B. Effect of serum albumin on siderophore-mediated utilization of transferring iron. *Biochem. J.* **10**, 2122–2127 (1984).
68. Nair, P. R. & Alam, M. A. Theory of “selectivity” of label-free nanobiosensors: A geometro-physical perspective. *J. Appl. Phys.* **107**, 064701 (2010).
69. Fan, R. *et al.* Integrated barcode chips for rapid, multiplexed analysis of proteins in microliter quantities of blood. *Nature Biotechnol.* **26**, 1373–1378 (2008).
70. Stern, E. *et al.* Label-free biomarker detection from whole blood. *Nature Nanotech.* **5**, 138–142 (2010).
- A two-stage detection approach leads to significantly enhanced specificity, enabling subpicomolar detection in whole blood with nanoribbon sensors.**
71. Hirrlinger, J., Moeller, H., Kirchoff, F. & Dringen, R. Expression of multidrug resistance proteins (Mrps) in astrocytes of the mouse brain: A single cell RT-PCR study. *Neurochem. Res.* **30**, 1237–1244 (2005).
72. Goluch, E. D. *et al.* A biobarcode assay for on-chip attomolar-sensitivity protein detection. *Lab Chip* **6**, 1293–1299 (2006).
73. Grell, M., Wajant, H., Zimmermann, G. & Scheurich, P. The type 1 receptor (CD120a) is the high-affinity receptor for soluble tumor necrosis factor. *Proc. Natl Acad. Sci. USA* **95**, 570–575 (1998).
74. Florin, E. L., Moy, V. T. & Gaub, H. E. Intermolecular forces and energies between ligands and receptors. *Science* **264**, 415–417 (1994).
75. Fritz, J., Katopodis, A. G., Kolbinger, F. & Anselmetti, D. Force-mediated kinetics of single P-selectin/ligand complexes observed by atomic force microscopy. *Proc. Natl Acad. Sci. USA* **95**, 12283–12288 (1998).
76. Merkel, R., Nassoy, P., Leung, A., Ritchie, K. & Evans, E. Energy landscapes of receptor-ligand bonds explored with dynamic force spectroscopy. *Nature* **397**, 50–53 (1999).
77. Wiita, A. P. *et al.* Probing the chemistry of thioredoxin catalysis with force. *Nature* **450**, 124–127 (2007).
78. Fernandez, J. M. & Hongbin, L. Force spectroscopy monitors the folding trajectory of a single protein. *Science* **303**, 1674–1678 (2004).
79. Tan, J. L. *et al.* Cells lying on a bed of microneedles: An approach to isolate mechanical force. *Proc. Natl Acad. Sci. USA* **100**, 1484–1489 (2003).
80. Guck, J. *et al.* Optical deformability as an inherent cell marker for testing malignant transformation and metastatic competence. *Biophys. J.* **88**, 3689–3698 (2005).



81. Suresh, S. Biomechanics and biophysics of cancer cells. *Acta Mater.* **55**, 3989–4014 (2007).
82. Lee, W., Fon, W., Axelrod, B. W. & Roukes, M. L. High-sensitivity microfluidic calorimeters for biological and chemical applications. *Proc. Natl Acad. Sci. USA* **106**, 15225–15230 (2009).
83. Cross, S. E., Jin, Y.-S., Rao, J. & Gimzewski, J. K. Nanomechanical analysis of cells from cancer patients. *Nature Nanotech.* **2**, 780–783 (2007).
84. Bruić, J., Hermans, R. I., Walthers, K. A. & Fernandez, J. M. Single-molecule force spectroscopy reveals signatures of glassy dynamics in the energy landscape of ubiquitin. *Nature Phys.* **2**, 282–286 (2006).
85. Evans, E., Leung, A., Heinrich, V. & Zhu, Ch. Mechanical switching and coupling between two dissociation pathways in a P-selectin adhesion bond. *Proc. Natl Acad. Sci. USA* **101**, 11281–11286 (2004).
86. Robert, P., Benoliel, A.-M., Pierres, A. & Bongrand, P. What is the biological relevance of the specific bond properties revealed by single-molecule studies? *J. Mol. Recognit.* **20**, 432–447 (2007).
87. Zhou, J. *et al.* Unbinding of the streptavidin-biotin complex by atomic force microscopy: a hybrid simulation study. *J. Chem. Phys.* **125**, 104905 (2006).
88. Evans, E. A. & Calderwood, D. A. Forces and bond dynamics in cell adhesion. *Science* **316**, 1148–1153 (2007).
89. Liphardt, J., Onoa, B., Smith, S. B., Tinoco, I. Jr & Bustamante, C. Reversible unfolding of single RNA molecules by mechanical force. *Science* **292**, 733–737 (2001).
90. Krieg, M. *et al.* Tensile forces govern germ-layer organization in zebrafish. *Nature Cell Biol.* **10**, 429–436 (2008).
91. Fierro, F. A. *et al.* BCR/ABL expression of myeloid progenitors increases beta1-integrin mediated adhesion to stromal cells. *J. Mol. Biol.* **377**, 1082–1093 (2008).
92. Wjckiewicz, E. *et al.* LFA-1 binding destabilizes the JAM-A homophilic interaction during leukocyte transmigration. *Biophys. J.* **96**, 285–293 (2009).
93. Friedrichs, J., Helenius, J. & Müller, D. J. Stimulated single-cell force spectroscopy to quantify cell adhesion receptor crosstalk. *Proteomics* **10**, 1455–1462 (2010).
94. Fon, W. C., Schwab, K. C., Worlock, J. M. & Roukes, M. L. Nanoscale, phonon-coupled calorimetry with sub-attojoule/Kelvin resolution. *Nano Lett.* **5**, 1968–1971 (2005).
95. Ekin, K. L. Electromechanical transducers at the nanoscale: actuation and sensing of motion in nanoelectromechanical systems (NEMS). *Small* **1**, 786–797 (2005).
96. Carr, D. W., Evoy, S., Sekaric, L., Craighead, H. G. & Parpia, J. M. Measurement of mechanical resonance and losses in nanometer scale silicon wires. *Appl. Phys. Lett.* **75**, 920–922 (1999).
97. Kouh, T., Karabacak, D., Kim, D. H. & Ekin, K. L. Diffraction effects in optical interferometric displacement detection in nanoelectromechanical systems. *Appl. Phys. Lett.* **86**, 013106 (2005).
98. Keeler, B. E. N., Carr, D. W., Sullivan, J. P., Friedmann, T. A. & Wendt, J. R. Experimental demonstration of a laterally deformable optical nanoelectromechanical system grating transducer. *Opt. Lett.* **29**, 1182–1184 (2004).
99. Li, M., Pernice, W. H. P. & Tang, H. X. Broadband all-photonic transduction of nanocantilevers. *Nature Nanotech.* **4**, 377–382 (2009).
100. Li, M. *et al.* Harnessing optical forces in integrated photonic circuits. *Nature* **467**, 480–484 (2008).
101. Truitt, P. A., Hertzberg, J. B., Huang, C. C., Ekin, K. L. & Schwab, K. C. Efficient and sensitive capacitive readout of nanomechanical resonator arrays. *Nano Lett.* **7**, 120–126 (2007).
102. Sampathkumar, A., Murray, T. W. & Ekin, K. L. Photothermal operation of high frequency nanoelectromechanical systems. *Appl. Phys. Lett.* **88**, 223104 (2006).
103. Verbridge, S. S., Bellan, L. M., Parpia, J. M. & Craighead, H. G. Optically driven resonance of nanoscale flexural oscillators in liquid. *Nano Lett.* **6**, 2109–2114 (2006).
104. Bargatin, I., Kokinsky, I. & Roukes, M. L. Efficient electrothermal actuation of multiple modes of high-frequency nanoelectromechanical resonators. *Appl. Phys. Lett.* **90**, 093116 (2007).
105. Seo, J. H. & Brand, O. High Q-factor in-plane-mode resonant microsensor platform for gaseous/liquid environment. *J. Microelectromech. Syst.* **17**, 483–493 (2008).
106. Piazza, G., Stephanou, P. J. & Pisano, A. P. Piezoelectric aluminum nitride vibrating contour-mode MEMS resonators. *J. Microelectromech. Syst.* **15**, 1406–1418 (2006).
107. Karabalin, R. B. *et al.* Piezoelectric nanoelectromechanical resonators based on aluminum nitride thin films. *Appl. Phys. Lett.* **95**, 103111 (2009).
108. Bargatin, I., Myers, E. B., Arlett, J., Gudlewski, B. & Roukes, M. L. Sensitive detection of nanomechanical motion using piezoresistive signal downmixing. *Appl. Phys. Lett.* **86**, 133109 (2005).
109. Harley, J. A. & Kenny, T. W. High-sensitivity piezoresistive cantilevers under 1000Å thick. *Appl. Phys. Lett.* **75**, 289–291 (1999).
110. Arlett, J. L., Maloney, J. R., Gudlewski, B., Muluneh, M. & Roukes, M. L. Self-sensing micro- and nanocantilevers with attonewton-scale force resolution. *Nano Lett.* **6**, 1000–1006 (2006).
111. Harley, J. A. & Kenny, T. W. 1/f noise considerations for the design and process optimization of piezoresistive cantilevers. *J. Microelectromech. Syst.* **9**, 226–235 (2000).
112. Li, M., Tang, H. X. & Roukes, M. L. Ultra-sensitive NEMS-based cantilevers for sensing, scanned probe and very high-frequency applications. *Nature Nanotech.* **2**, 114–120 (2007).
113. Nguyen, C. T.-C. & Howe, R. T. An integrated CMOS micromechanical resonator high-Q oscillator. *IEEE J. Solid-St. Circ.* **34**, 440–455 (1999).
114. Despont, M., Drechsler, U., Yu, R., Pogge, H. B. & Vettiger, P. Wafer-scale microdevice transfer/interconnect: its application in an AFM-based data-storage system. *J. Microelectromech. Syst.* **13**, 895–901 (2004).
115. Thorsen, T., Maerkl, S. J. & Quake, S. R. Microfluidic large-scale integration. *Science* **298**, 580–584 (2002).
116. Zhong, J. F. *et al.* A microfluidic processor for gene expression profiling of single human embryonic stem cells. *Lab Chip* **8**, 68–74 (2008).
117. Gómez-Sjöberg, R., Leyrat, A. A., Pirone, D. M., Chen, C. S. & Quake, S. R. Versatile, fully automated, microfluidic cell culture system. *Anal. Chem.* **79**, 8557–8563 (2007).
118. Mehta, A. I. *et al.* Biomarker amplification by serum carrier protein binding. *Dis. Markers* **19**, 1–10 (2003).
119. Granger, J., Siddiqui, J., Copeland, S. & Remick, D. Albumin depletion of human plasma also removes low abundance proteins including the cytokines. *Proteomics* **5**, 4713–4718 (2005).
120. Köster, R. *et al.* Drop-based microfluidic devices for encapsulation of single cells. *Lab Chip* **8**, 1110–1115 (2008).
121. Pradines-Figueres, A. & Raetz, C. R. H. Processing and secretion of tumor necrosis factor  $\alpha$  in endotoxin-treated Mono Mac 6 cells are dependent on phorbol myristate acetate. *J. Biol. Chem.* **267**, 23261–23268 (1992).
122. Huber, F. *et al.* Analyzing gene expression using combined nanomechanical cantilever sensors. *J. Phys.: Conf. Ser.* **61**, 450–453 (2007).
123. McKendry, R. *et al.* Multiple label-free biodetection and quantitative DNA-binding assays on a nanomechanical cantilever array. *Proc. Natl Acad. Sci. USA* **99**, 9783–9788 (2002).
124. Huber, F., Hegner, M., Gerber, C., Güntherodt, H.-J. & Lang, H. P. Label free analysis of transcription factors using microcantilever arrays. *Biosens. Bioelectron.* **21**, 1599–1605 (2006).
125. Bietsch, A., Hegner, M., Lang, H. P. & Gerber, C. Inkjet deposition of alkanethiolate monolayers and DNA Oligonucleotides on gold: evaluation of spot uniformity by wet etching. *Langmuir* **20**, 5119–5122 (2004).
126. Zhang, H., Lee, K. B., Li, Z. & Mirkin, C. A. Biofunctionalized nanoarrays of inorganic structures prepared by dip-pen nanolithography. *Nanotechnology* **14**, 1113–1117 (2003).
127. Harper, J. C., Polsky, R., Dirk, S. M., Wheeler, D. R. & Brozik, S. M., Electroaddressable selective functionalization of electrode arrays: Catalytic NADH detection using aryl diazonium modified gold electrodes. *Electroanalysis* **19**, 1268–1274 (2007).
128. Zheng, G., Patolsky, F., Cui, Y., Wang, W. U. & Lieber, C. M. Multiplexed electrical detection of cancer markers with nanowire sensor arrays. *Nature Biotechnol.* **23**, 1294–1301 (2005).
129. Lipsitz, R. Diagnostics at home: Pregnancy tests. *Sci. Amer.* **283**, 110–111 (November 2000).
130. Washburn, A. L., Gunn, L. C. & Bailey, R. C. Label-free quantitation of a cancer biomarker in complex media using silicon photonic microring resonators. *Anal. Chem.* **81**, 9499–9506 (2009).
131. Viani, M. B. *et al.* Small cantilevers for force spectroscopy of single molecules. *J. Appl. Phys.* **86**, 2258–2262 (1999).
132. Arlett, J. L. *et al.* BioNEMS: Nanomechanical systems for single-molecule biophysics. *Lect. Notes Phys.* **711**, 241–270 (2007).

## Acknowledgements

The authors thank the Defense Advanced Research Projects Agency (HR00110610043 and N66001-08-1-2043) and the Fondation pour la Recherche et l'Enseignement Supérieur for support. M.L.R. acknowledges a Director's Pioneer Award from the National Institutes of Health (1DP1OD006924). We also thank P. Puget for many discussions.

## Additional information

The authors declare no competing financial interests.